

# Adaptive and Pressure-Robust Discretization of Incompressible Pressure-Driven Phase-Field Fracture

Seshadri Basava and Katrin Mang and Mirjam Walloth and Thomas Wick and Winnifried Wollner

**Abstract** In this work, we consider pressurized phase-field fracture problems in nearly and fully incompressible materials. To this end, a mixed form for the solid equations is proposed. To enhance the accuracy of the spatial discretization, a residual-type error estimator is developed. Our algorithmic advancements are substantiated with several numerical tests that are inspired from benchmark configurations. Therein, a primal-based formulation is compared to our newly developed mixed phase-field fracture method for Poisson ratios approaching  $\nu \rightarrow 0.5$ . Finally, for  $\nu = 0.5$ , we compare the numerical results of the mixed formulation with a pressure robust modification.

## 1 Introduction

This work is devoted to pressurized fractures in nearly and fully incompressible solids using an adaptive finite element discretization. Pressurized fracture problems modeled with a phase-field method is currently a topic being investigated by many groups; see for instance [46, 12, 33, 20, 27], to name a few. We further extended our pressurized phase-field fracture approach to non-isothermal configurations [39].

---

Seshadri Basava

Technische Universität Darmstadt e-mail: basava@mathematik.tu-darmstadt.de

Katrin Mang

Leibniz Universität Hannover e-mail: mang@ifam.uni-hannover.de

Mirjam Walloth

Technische Universität Darmstadt e-mail: walloth@mathematik.tu-darmstadt.de

Thomas Wick

Leibniz Universität Hannover e-mail: thomas.wick@ifam.uni-hannover.de

Winnifried Wollner

Technische Universität Darmstadt e-mail: wollner@mathematik.tu-darmstadt.de

A recent overview on pressurized and fluid-filled fractures is provided in [47]. However, all these contributions deal with compressible solids in which Poisson's ratio is significantly less than 0.5, i.e., the incompressible limit.

Incompressible solids are however an important field in solids mechanics [23, 43, 24, 40, 26]. In [32] a model and robust discretization using a phase-field method for fractures in solids mechanics was proposed. A well-known challenge in phase-field methods is the relationship between the model regularization  $\varepsilon > 0$  and the spatial mesh size  $h$ . To obtain accurate discretizations for small  $\varepsilon$  around the fracture and specifically at the fracture tip adaptive mesh refinement is a useful tool. First studies date back to [10, 11] investigating residual-type error estimators. A predictor-corrector mesh refinement algorithm with a focus on crack-oriented refinement was developed in [21] and extended to three spatial dimensions in [27]. In [4], anisotropic mesh refinement was studied. Goal-oriented adjoint-based a posteriori error estimation was subject in [48]. Based on a recent approach for residual-type a posteriori estimators for contact problems [25, 45] we developed in [44] a reliable and efficient estimator for a singularly-perturbed obstacle problem taking into account the robustness (in terms of  $\varepsilon$ ). We tested the resulting residual-type estimator for different fracture phase-field problems enforcing the irreversibility condition in [30] and further for nearly incompressible solids in [31].

The main objective of the current work is two-fold. We first develop a phase-field model using a mixed system for pressurized fractures. Therein the methodology from [32] is combined with pressurized fractures as proposed in [36, 35, 46]. Our second aim is to apply adaptive refinement based on our residual-type error estimator [30, 44] to this mixed-system phase-field fracture approach. These algorithmic concepts are substantiated with the help of several numerical examples and mesh convergence studies comparing classical primal formulations and our newly developed mixed formulation. Finally, we will test a pressure-robust modification of the discrete mixed formulation, inspired by the works [28, 29] for the Stokes problem.

As this book chapter summarizes our efforts within the German Priority Programme 1748 (DFG SPP 1748), in the project 'Structure Preserving Adaptive Enriched Galerkin Methods for Pressure-Driven 3D Fracture Phase-Field Models', we briefly mention the other research directions, which were related to our own overall goal.

In [9], we considered a stabilized decoupled iteration scheme, a so-called  $L$ -scheme. Therein constant stabilization parameters were introduced including both numerical analysis and computational verification. An enhancement in efficiency by using dynamically chosen stabilization parameters during the iteration was subsequently proposed in [15]. We published our open-source parallel computing paper with heuristic adaptive mesh refinement [22]. The open-source programming code was used in the SPP benchmark collection [50]. Several comparisons of different stress-splitting methods were done in [16].

The predictor-corrector approach from [21] inspired an adaptive non-intrusive global-local approach in [38], a paper, which is also a collaboration within the SPP 1748 with the group of Peter Wriggers.

In the work [44] the basis for a provably reliable and efficient error estimator for fracture phase-field models has been set. The resulting residual-type error estimator has been used to steer solely the adaptive refinement and thus the resolution of the critical region around the crack without any prior knowledge about the problem in [30, 31].

The outline of this paper is as follows. In Section, 2 the notation and equations are introduced. Next, in Section 3, both the discretization and the numerical solution are addressed. In Section 4, a residual-type error estimator for pressurized fractures is presented. In the final Section 5 several numerical tests are conducted. We summarize our findings in Section 6.

## 2 Notation and equations

In this section, we introduce the basic notation and the underlying equations. In the following, let  $\Omega \subset \mathbb{R}^2$  the total domain wherein  $C \subset \mathbb{R}$  denotes the fracture and  $\widehat{\Omega} \subset \mathbb{R}^2$  is the intact domain. The outer boundary is denoted by  $\partial\Omega$ . The inner fracture boundary is denoted by  $\partial\widehat{\Omega}_F = C$ .

Using a phase-field approach, the one-dimensional fracture  $C$  is approximated on  $\Omega \in \mathbb{R}^2$  with the help of an elliptic (Ambrosio-Tortorelli) functional [1, 2]. This yields an approximate inner fracture boundary  $\partial\Omega_F \approx C$ . For fracture formulations posed in a variational setting, this has been first proposed in [6] based on the model developed in [18]. Finally, we denote the  $L^2$  scalar product with  $(\cdot, \cdot)$  as frequently used in the literature.

Variational phase-field fracture starts with an energy functional and the motion of the body under consideration is then determined by the Euler-Lagrange equations, which are obtained by differentiation with respect to the unknowns. Therefore, in phase-field-based fracture propagation, the unknown solution variables are vector-valued displacements  $u : \Omega \rightarrow \mathbb{R}^2$  and a smoothed scalar-valued indicator phase-field function  $\varphi : \Omega \rightarrow [0, 1]$ . Here  $\varphi = 0$  denotes the crack region and  $\varphi = 1$  characterizes the unbroken material. The intermediate values constitute a smooth transition zone dependent on a regularization parameter  $\varepsilon$ . The physics of the underlying problem ask to enforce a crack irreversibility condition (the crack can never heal) yielding the inequality constraint

$$\varphi \leq \varphi^{n-1}.$$

Here,  $\varphi^{n-1}$  denote the previous time step solution and  $\varphi$  the current solution.

### 2.1 Pressurized phase-field fracture in a displacement formulation

In this work, we are specifically interested in pressurized fractures in which a given pressure acts on the fracture boundary  $\partial\Omega_F$ . Using classical interface coupling conditions, namely kinematic and dynamic coupling conditions, for the pressure

and balance of contact forces, a pressure  $p_g$  can be prescribed. However, due to the smeared zone of size  $\varepsilon$  in which  $0 < \varphi < 1$ , the exact location of the fracture interface is not known and leaves some freedom where to put it. In [35][Section 2] or [36][Section 3.2], we used the divergence theorem to transform  $p_g$  from  $\partial\Omega_F$  into the entire domain  $\Omega$ . This procedure avoids knowledge of the exact fracture boundary location, but is mathematically rigorous. Mathematical analysis ([35],[36]) and numerous computations, e.g., in [46, 22, 50], have shown that this approach is justified. As a consequence of the transformation, the pressure  $p_g : \Omega \rightarrow \mathbb{R}$  is added as domain integral to the Euler-Lagrange equations.

Let  $V := H_0^1(\Omega; \mathbb{R}^2)$  and  $W := H^1(\Omega)$  the usual Hilbert spaces and the convex set

$$K := K^n = \{w \in W \mid w \leq \varphi^{n-1} \leq 1 \text{ a.e. on } \Omega\}$$

including the inequality constraint.

The Euler-Lagrange system for pressurized phase-field fracture reads [36]:

**Problem 1** Let  $p_g \in W^{1,\infty}(\Omega)$  be given. For the loading steps  $n = 1, 2, 3, \dots, N$ : Find vector-valued displacements and a scalar-valued phase-field variable  $\{u, \varphi\} := \{u^n, \varphi^n\} \in V \times W$  such that

$$\left( g(\varphi) \sigma(u), e(v) \right) + (\varphi^2 p_g, \operatorname{div} v) + (\varphi^2 \nabla p_g, v) = 0 \quad \forall v \in V, \quad (1)$$

and

$$\begin{aligned} & (1 - \kappa)(\varphi \sigma(u) : e(u), \psi - \varphi) \\ & + 2(\varphi p_g \operatorname{div} u, \psi - \varphi) + 2(\varphi \nabla p_g \cdot u, \psi - \varphi) \\ & + G_c \left( -\frac{1}{\varepsilon} (1 - \varphi, \psi - \varphi) + \varepsilon (\nabla \varphi, \nabla(\psi - \varphi)) \right) \geq 0 \quad \forall \psi \in K. \end{aligned} \quad (2)$$

Here,

$$g(\varphi) = ((1 - \kappa)\varphi^2 + \kappa)$$

is the so-called degradation function with a small regularization parameter  $\kappa$ ,  $G_c$  is the critical energy release rate, and we use the well-known Hook's law for the linear stress-strain relationship of isotropic materials:

$$\sigma(u) := 2\mu e(u) + \lambda \operatorname{tr} e(u) \mathbf{I}, \quad (3)$$

where  $\mu$  and  $\lambda$  denote the Lamé coefficients,  $e(u) = \frac{1}{2}(\nabla u + \nabla u^T)$  is the linearized strain tensor and  $\mathbf{I}$  is the identity matrix.

## 2.2 Pressurized phase-field fracture in a mixed formulation

Following [32], we now derive a mixed formulation for pressurized fractures. To this end, we need to split the stress tensor (3) into the shear part and the volumetric

part. In nearly incompressible materials with Poisson's ratio going to 0.5, for the volumetric parameter, it holds

$$\lambda \rightarrow \infty.$$

To cope with volumetric locking, one possibility is to introduce a Lagrange multiplier, e.g., [7], with  $p \in P := L^2(\Omega)$  such that

$$p := \lambda \operatorname{tr} e(u).$$

*Remark 1* This solution variable  $p$  should not be confused with the given pressure  $p_g$  from before.

With that, we obtain for the stress tensor:

$$\sigma(u, p) := 2\mu e(u) + p \mathbf{I},$$

as it has been analyzed in our work [32] without the given pressure  $p_g$ . Adding this fracture pressure  $p_g$ , we obtain the following reformulation:

**Problem 2** Let  $p_g \in W^{1,\infty}(\Omega)$  be given. For the loading steps  $n = 1, 2, 3, \dots, N$ : Find vector-valued displacements, a scalar-valued pressure, and a scalar-valued phase-field variable  $\{u, p, \varphi\} := \{u^n, p^n, \varphi^n\} \in V \times P \times W$  such that

$$\left( g(\varphi) \sigma(u, p), e(v) \right) + (\varphi^2 p_g, \operatorname{div} v) + (\varphi^2 \nabla p_g, v) = 0 \quad \forall v \in V, \quad (4)$$

and

$$(\operatorname{tr} e(u), q) - \frac{1}{\lambda}(p, q) = 0 \quad \forall q \in P, \quad (5)$$

and

$$\begin{aligned} & (1 - \kappa)(\varphi \sigma(u, p) : e(u), \psi - \varphi) \\ & + 2(\varphi p_g \operatorname{div} u, \psi - \varphi) + 2(\varphi \nabla p_g \cdot u, \psi - \varphi) \\ & + G_c \left( -\frac{1}{\varepsilon}(1 - \varphi, \psi - \varphi) + \varepsilon(\nabla \varphi, \nabla(\psi - \varphi)) \right) \geq 0 \quad \forall \psi \in K. \end{aligned} \quad (6)$$

### 3 Discrete formulation

As the structure remains the same for all time steps, we consider one time step  $n$  for simplicity. For the discretization in space, we decompose the polygonal domain  $\Omega$  by a (family of) meshes  $\mathcal{M} = \mathcal{M}^n$  consisting of shape regular rectangles  $\epsilon$ , such that all meshes share a common coarse mesh. To allow for local refinement, in particular of rectangular elements, we allow for one hanging node per edge at which degrees of freedom will be eliminated to assert  $H^1$ -conformity of the discrete spaces. To each mesh, we associate the mesh size function  $h$ , i.e.,  $h|_{\epsilon} = h_{\epsilon} = \operatorname{diam} \epsilon$  for any element

$e \in \mathcal{M}$ . The set of nodes  $q$  is given by  $\mathcal{N}$  and we distinguish between the set  $\mathcal{N}^\Gamma$  of nodes at the boundary and the set of interior nodes  $\mathcal{N}^I$ . Later on, for the derivation of the estimator, we need the following definitions.

For a point  $q \in \mathcal{N}$ , we define a patch  $\omega_q$  as the interior of the union of all elements sharing the node  $q$ . We call the union of all sides in the interior of  $\omega_q$ , not including the boundary of  $\omega_q$ , skeleton and denote it by  $\gamma_q^I$ . For boundary nodes, we denote the intersections between  $\Gamma$  and  $\partial\omega_q$  by  $\gamma_q^\Gamma := \Gamma \cap \partial\omega_q$ . Further, we will make use of  $\omega_s$  which is the union of all elements sharing a side  $s$ . We need the definition of the jump term  $[\nabla\psi_h] := \nabla|_e\psi_h \cdot n_e - \nabla|_{\tilde{e}}\psi_h \cdot n_e$  where  $e, \tilde{e}$  are neighboring elements and  $n_e$  is the unit outward normal on the common side of the two elements. For the discretization, we consider (bi)-linear ( $\mathbb{Q}_1(e)$ ), (bi)-quadratic ( $\mathbb{Q}_2(e)$ ) and linear ( $\mathbb{P}_1(e)$ ) shape functions. Thus, the finite element spaces are given by

$$\begin{aligned} W_h &:= W_h^n = \{v_h \in C^0(\overline{\Omega}) \mid \forall e \in \mathcal{M}, v_h|_e \in \mathbb{Q}_1(e)\} \subset W, \\ P_h &:= P_h^n = \{p_h \in P \mid \forall e \in \mathcal{M}, p_h|_e \in \mathbb{P}_1(e)\} \subset P, \end{aligned}$$

and by

$$V_h := V_h^n = \{v_h \in C^0(\overline{\Omega}; \mathbb{R}^2) \mid \forall e \in \mathcal{M}, v_h|_e \in \mathbb{Q}_1(e)^2 \text{ and } v_h = 0 \text{ on } \Gamma\} \subset V$$

for the discrete analog of Problem 1 and by

$$V_h := V_h^n = \{v_h \in C^0(\overline{\Omega}; \mathbb{R}^2) \mid \forall e \in \mathcal{M}, v_h|_e \in \mathbb{Q}_2(e)^2 \text{ and } v_h = 0 \text{ on } \Gamma\} \subset V,$$

for the discrete analog of Problem 2, respectively.

We define the respective nodal interpolation operators as  $I_h^n$ , and define the discrete feasible set for the phase-field by

$$K_h := K_h^n = \{\psi_h \in W_h \mid \psi_h(q) \leq (I_h^n \varphi_h^{n-1})(q), \quad \forall q \in \mathcal{N}\}.$$

The nodal basis functions of the finite element space  $W_h$  are denoted by  $\phi_q$ .

Analogous to Problem 1, we define the spatially discretized time step problem:

**Problem 3 (Discrete formulation of Problem 1)** Let  $p_g \in W^{1,\infty}(\Omega)$  be given. For the loading steps  $n = 1, 2, 3, \dots, N$ : Find vector-valued displacements and a scalar-valued phase-field variable  $\{u_h, \varphi_h\} := \{u_h^n, \varphi_h^n\} \in V_h \times W_h$  such that

$$\left( g(\varphi_h) \sigma(u_h), e(v_h) \right) + (\varphi_h^2 p_g, \operatorname{div} v_h) + (\varphi_h^2 \nabla p_g, v_h) = 0 \quad \forall v_h \in V_h, \quad (7)$$

and

$$\begin{aligned} &(1 - \kappa)(\varphi_h \sigma(u_h) : e(u_h), \psi_h - \varphi_h) \\ &+ 2(\varphi_h p_g \operatorname{div} u_h, \psi_h - \varphi_h) + 2(\varphi_h \nabla p_g \cdot u_h, \psi_h - \varphi_h) \\ &+ G_c \left( -\frac{1}{\varepsilon} (1 - \varphi_h, \psi_h - \varphi_h) + \varepsilon (\nabla \varphi_h, \nabla(\psi_h - \varphi_h)) \right) \geq 0 \quad \forall \psi \in K. \end{aligned} \quad (8)$$

Analogous to Problem 2, we define the spatially discretized mixed time step problem:

**Problem 4 (Discrete formulation of Problem 2)** Let  $p_g \in W^{1,\infty}(\Omega)$  be given. For the loading steps  $n = 1, 2, 3, \dots, N$ : Find vector-valued displacements, a scalar-valued pressure, and a scalar-valued phase-field variable  $\{u_h, p_h, \varphi_h\} := \{u_h^n, p_h^n, \varphi_h^n\} \in V_h \times P_h \times W_h$  such that

$$\begin{aligned} & \left( g(\varphi_h) \sigma(u_h, p_h), e(v_h) \right) + (\varphi_h^2 p_g, \operatorname{div} v_h) \\ & + (\varphi_h^2 \nabla p_g, v_h) = 0 \quad \forall v_h \in V_h, \end{aligned} \quad (9)$$

and

$$(\operatorname{tr} e(u_h), q_h) - \frac{1}{\lambda} (p_h, q_h) = 0 \quad \forall q_h \in P_h, \quad (10)$$

and

$$\begin{aligned} & (1 - \kappa)(\varphi_h \sigma(u_h, p_h) : e(u_h), \psi_h - \varphi_h) \\ & + 2(\varphi_h p_g \operatorname{div} u_h, \psi_h - \varphi_h) + 2(\varphi_h \nabla p_g \cdot u_h, \psi_h - \varphi_h) \\ & + G_c \left( -\frac{1}{\varepsilon} (1 - \varphi_h, \psi_h - \varphi_h) + \varepsilon (\nabla \varphi_h, \nabla (\psi_h - \varphi_h)) \right) \geq 0 \quad \forall \psi_h \in K_h. \end{aligned} \quad (11)$$

Finally, following the work of [28, 29], we propose a pressure robust modification of Problem 4. To this end, we define the divergence conforming space of Raviart-Thomas finite elements, see, e.g., [8, Section III.3.2], on the unit square  $(-1, 1)^2$  by

$$\mathbb{RT}_1 = \mathbb{Q}_1^2 + \mathbf{x}\mathbb{Q}_1.$$

As usual, for elements  $e \in \mathcal{M}$ , the space

$$\mathbb{RT}_1(e)$$

is then obtained by mapping of the shape functions utilizing a Piola transform. With this, we can define the global space

$$\widehat{V}_h = \{v_h \in C^0(\overline{\Omega}; \mathbb{R}^2) \mid \forall e \in \mathcal{M}, v_h|_e \in \mathbb{RT}_1(e)\}$$

together with the interpolation operator  $I_{\mathbb{RT}}: V_h \rightarrow \widehat{V}_h$ . Now, following [28, 29], the pressure robust reformulation of Problem 4 is the problem

**Problem 5 (Pressure robust formulation of Problem 4)** Let  $p_g \in W^{1,\infty}(\Omega)$  be given. For the loading steps  $n = 1, 2, 3, \dots, N$ : Find vector-valued displacements, a scalar-valued pressure, and a scalar-valued phase-field variable  $\{u_h, p_h, \varphi_h\} := \{u_h^n, p_h^n, \varphi_h^n\} \in V_h \times P_h \times W_h$  such that

$$\begin{aligned} & \left( g(\varphi_h) \sigma(u_h, p_h), e(v_h) \right) + (\varphi_h^2 p_g, \operatorname{div} I_{\mathbb{RT}} v_h) \\ & + (\varphi_h^2 \nabla p_g, I_{\mathbb{RT}} v_h) = 0 \quad \forall v_h \in V_h, \end{aligned} \quad (12)$$

as well as (10) and (11) hold.

#### 4 Residual-type a posteriori error estimator

We propose an estimator for the phase-field inequality (8) or (11), respectively, to obtain a good resolution of the fracture growth.

Utilizing either  $\sigma_h^n := \sigma(u_h^n, p_h^n)$  for the mixed form or  $\sigma_h^n := \sigma(u_h^n)$  for the non-mixed form, we introduce the bilinear form

$$a_{h,\epsilon}(\zeta, \psi) := \frac{G_c}{\epsilon}(\zeta, \psi) + (1 - \kappa)(\sigma_h^n : e(u_h^n) \zeta, \psi) \\ + 2(p_g \operatorname{div} u_h^n \zeta, \psi) + 2(\nabla p_g \cdot u_h^n \zeta, \psi) + G_c \epsilon (\nabla \zeta, \nabla \psi). \quad (13)$$

Thus, the discretized variational inequality in a time step  $n$  is given by

**Problem 6 (Discrete variational inequality)** Let  $u_h^n, p_h^n$  and  $\varphi_h^{n-1}$  be given, then find  $\varphi_h \in K_h$  such that

$$a_{h,\epsilon}(\varphi_h, \psi_h - \varphi_h) \geq \frac{G_c}{\epsilon} (1, \psi_h - \varphi_h) \quad \forall \psi_h \in K_h. \quad (14)$$

We define the discrete constraining force density  $\Lambda_h \in W_h^*$  of Problem 6 as

$$\langle \Lambda_h, \psi_h \rangle_{-1,1} := \frac{G_c}{\epsilon} (1, \psi_h) - a_{h,\epsilon}(\varphi_h, \psi_h) \quad \forall \psi_h \in W_h. \quad (15)$$

The solution of Problem 6 is the discrete approximation of the auxiliary problem:

**Problem 7** Let  $u_h^n, p_h^n$  and  $\varphi_h^{n-1}$  be given, then find

$$\hat{\varphi} \in K(I_h^n(\varphi_h^{n-1})) := \{\psi \in W \mid \psi \leq I_h^n(\varphi_h^{n-1})\}$$

such that

$$a_{h,\epsilon}(\hat{\varphi}, \psi - \hat{\varphi}) \geq \frac{G_c}{\epsilon} (1, \psi - \hat{\varphi}) \quad \forall \psi \in K(I_h^n(\varphi_h^{n-1})). \quad (16)$$

The corresponding constraining force density  $\hat{\Lambda} \in W^*$  of Problem 7 is

$$\langle \hat{\Lambda}, \psi \rangle_{-1,1} := \frac{G_c}{\epsilon} (1, \psi) - a_{h,\epsilon}(\hat{\varphi}, \psi) \quad \forall \psi \in W.$$

*Remark 2* As the bilinear form  $a_{h,\epsilon}(\cdot, \cdot)$  depends on the approximation  $u_h^n$  of  $u^n$  and  $p_h^n$  of  $p^n$  and the constraints depend on the approximation  $I_h^n(\varphi_h^{n-1})$  of  $\varphi^{n-1}$ , the solution  $\hat{\varphi}$  of (16) is an approximation to the solution  $\varphi^n$  of (2) or (6), respectively.

Assuming we knew  $\hat{\Lambda}$  then



$$\langle R(\varphi_h), \psi \rangle_{-1,1} := \langle -\hat{\Lambda}, \psi \rangle_{-1,1} + \frac{G_c}{\epsilon} (1, \psi) - a_{h,\epsilon}(\varphi_h, \psi)$$

defines the linear residual to the corresponding equation. Thus,  $R(\varphi_h) = 0$  if and only if  $\varphi_h = \hat{\varphi}$ . Further, we are interested in the error in the constraining forces. As  $\Lambda_h$  is not a functional on  $W$ , but a functional on  $W_h$ , it is not uniquely defined how  $\Lambda_h$  acts on  $W$ . Thus, to compare the constraining force  $\hat{\Lambda} \in W^*$  with a discrete counterpart, we choose a functional on  $W^*$  called quasi-discrete constraining force, denoted by  $\tilde{\Lambda}_h \in W^*$ . Therefore, we follow the approach used in [17, 37, 25, 44] and distinguish between full-contact nodes  $q \in \mathcal{N}^{fC}$  and semi-contact nodes  $q \in \mathcal{N}^{sC}$ . Full-contact nodes are those nodes for which the solution is fixed to the obstacle  $\varphi_h = I_h^n(\varphi_h^{n-1})$  on  $\omega_q$  and the sign condition  $\langle \Lambda_h, \psi \rangle_{-1,1,\omega_q} \geq 0 \forall \psi \geq 0 \in H_0^1(\omega_q)$  is fulfilled. Semi-contact nodes are those nodes for which  $\varphi_h(q) = I_h^n(\varphi_h^{n-1})(q)$  holds but not the conditions of full-contact. Based on this classification, we define the quasi-discrete constraining force, where  $\phi_q$  denotes the nodal basis of  $W_h$ ,

$$\langle \tilde{\Lambda}_h, \psi \rangle_{-1,1} := \sum_{q \in \mathcal{N}^{sC}} \langle \tilde{\Lambda}_h^q, \psi \phi_q \rangle_{-1,1} + \sum_{q \in \mathcal{N}^{fC}} \langle \tilde{\Lambda}_h^q, \psi \phi_q \rangle_{-1,1}, \quad (17)$$

with the local contributions which are for full-contact nodes

$$\langle \tilde{\Lambda}_h^q, \psi \phi_q \rangle_{-1,1} := \langle \Lambda_h, \psi \phi_q \rangle_{-1,1}$$

and for semi-contact nodes

$$\langle \tilde{\Lambda}_h^q, \psi \phi_q \rangle_{-1,1} := \langle \Lambda_h, \phi_q \rangle_{-1,1} c_q(\psi)$$

with  $c_q(\psi) = \frac{\int_{\tilde{\omega}_q} \psi \phi_q}{\int_{\tilde{\omega}_q} \phi_q}$ , where  $\tilde{\omega}_q$  is a proper subset of  $\omega_q$ . Therefore, we define the so-called Galerkin functional

$$\begin{aligned} \langle G, \psi \rangle_{-1,1} &:= \langle R(\varphi_h), \psi \rangle_{-1,1} + \langle \hat{\Lambda} - \tilde{\Lambda}_h, \psi \rangle_{-1,1} \\ &= \left( \frac{G_c}{\epsilon}, \psi \right) - \langle \tilde{\Lambda}_h, \psi \rangle_{-1,1} - a_{h,\epsilon}(\varphi_h, \psi). \end{aligned}$$

We note that in the case that  $p_g = \text{const}$  and  $\text{div}(u_h^n) = 0$ , i.e., the material is incompressible, the bilinear form  $a_{h,\epsilon}(\zeta, \psi)$  defined in (13) is elliptic; and the corresponding energy norm is given by

$$\| \cdot \|_\epsilon := \left\{ G_c \epsilon \|\nabla(\cdot)\|^2 + \left\| \left( \frac{G_c}{\epsilon} + (1 - \kappa) \sigma(u_h^n) : e(u_h^n) \right)^{\frac{1}{2}} (\cdot) \right\|^2 \right\}^{\frac{1}{2}}. \quad (18)$$

We denote the corresponding dual norm by  $\| \cdot \|_{*,\epsilon} := \frac{\sup_{\psi \in W} \langle \cdot, \psi \rangle_{-1,1}}{\| \psi \|_\epsilon}$ .

For the definition of the error estimator contributions, we use the abbreviation of the interior residual

$$r(\varphi_h) := \frac{G_c}{\epsilon} + G_c \epsilon \Delta \varphi_h - \frac{G_c}{\epsilon} \varphi_h - (1 - \kappa)(\sigma_h^n : e(u_h^n)) \varphi_h + 2p_g \operatorname{div} u_h^n \varphi_h + 2\nabla p_g \cdot u_h^n \varphi_h \quad (19)$$

and set

$$\alpha_q := \min_{x \in \omega_q} \left\{ \frac{G_c}{\epsilon} + (1 - \kappa)(\sigma(u_h^n) : e(u_h^n)) \right\}. \quad (20)$$

Deriving an upper bound of  $\|G\|_{*,\epsilon}$  as, e.g., in [44], we end up with the error indicator  $\eta$  which is the sum of the following contributions

$$\eta_1^2 := \sum_{q \in \mathcal{N} \setminus \mathcal{N}^{FC}} \eta_{1,q}^2, \quad \eta_{1,q} := \min \left\{ \frac{h_q}{\sqrt{G_c \epsilon}}, \alpha_q^{-\frac{1}{2}} \right\} \|r(\varphi_h)\|_{\omega_q} \quad (21)$$

$$\eta_2^2 := \sum_{q \in \mathcal{N} \setminus \mathcal{N}^{FC}} \eta_{2,q}^2, \quad \eta_{2,q} := \min \left\{ \frac{h_q}{\sqrt{G_c \epsilon}}, \alpha_q^{-\frac{1}{2}} \right\}^{\frac{1}{2}} (G_c \epsilon)^{-\frac{1}{4}} \|G_c \epsilon [\nabla \varphi_h]\|_{\gamma_q^I} \quad (22)$$

$$\eta_3^2 := \sum_{q \in \mathcal{N} \setminus \mathcal{N}^{FC}} \eta_{3,q}^2, \quad \eta_{3,q} := \min \left\{ \frac{h_q}{\sqrt{G_c \epsilon}}, \alpha_q^{-\frac{1}{2}} \right\}^{\frac{1}{2}} (G_c \epsilon)^{-\frac{1}{4}} \|G_c \epsilon \nabla \varphi_h\|_{\gamma_q^N} \quad (23)$$

In the case that  $p_g = \text{const}$  and the material is incompressible  $\operatorname{div}(u_h^n) = 0$ , we can derive a robust upper bound of the error measure

$$\|\hat{\varphi} - \varphi_h\|_{\epsilon} + \|\hat{\Lambda} - \tilde{\Lambda}_h\|_{*,\epsilon} \quad (24)$$

in terms of the estimator

$$\eta := \sum_{k=1}^4 \eta_k \quad (25)$$

which consists of the estimator contributions (21), (22), (23) and

$$\eta_4^2 := \sum_{q \in \mathcal{N}^{SC}} \eta_{4,q}^2, \quad \eta_{4,q} := s_q \int_{\tilde{\omega}_q} (I_h^n(\varphi_h^{n-1}) - \varphi_h) \phi_q.$$

**Theorem 1 (Reliability)** *Assuming that  $p_g = \text{const}$  and  $\operatorname{div}(u_h^n) = 0$ , the error estimator  $\eta$  provides a robust upper bound of the error measure, i.e.*

$$\|\hat{\varphi} - \varphi_h\|_{\epsilon} + \|\hat{\Lambda} - \tilde{\Lambda}_h\|_{*,\epsilon} \leq C \eta$$

*otherwise the estimator constitutes an upper bound of the dual norm of the Galerkin functional*

$$\|G\|_{*,\epsilon} \leq C \eta,$$

*where  $C$  does not depend on  $\epsilon$ .*

If  $p_g = \text{const}$  and  $\text{div}(u_h^n) = 0$ , the local estimator contributions constitute local lower bounds with respect to the local error measure (24). The proof to show reliability as well as efficiency follows the ideas of [44].

## 5 Numerical tests

In this section, we investigate some examples all motivated by the theoretical calculations of Sneddon [41] and Sneddon and Lowengrub [42] considering a pressure-driven cavity.

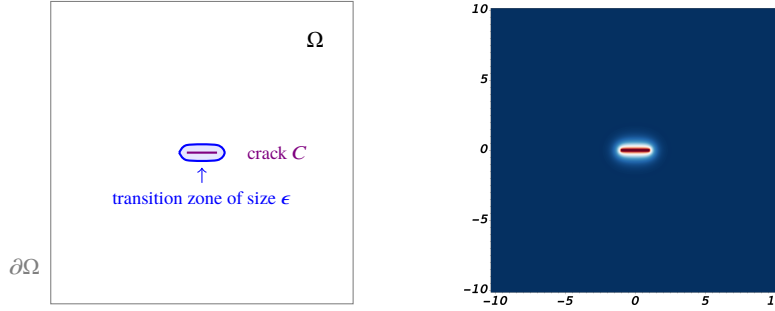


Fig. 1: Domain  $\Omega$  (in 2D) with Dirichlet boundaries  $\partial\Omega$ , an initial crack  $C$  of length  $2l_0$  and a crack width  $\epsilon$ , where the phase-field function  $\varphi$  is defined.

Our implementation is based on the open-source software DOpElib [19] and the finite elements from deal.II [3, 5]. The refinement strategy follows [30][Section 4.2]. This strategy allows to flag certain cells based on the cell-wise error indicators to reach a grid that is optimal with respect to an objective function that tries to balance reducing the error and increasing the numerical cost due to the added unknowns.

### Setup

We follow the setup from [50], where the case  $\nu = 0.2$  is discussed. We assume a two-dimensional domain  $\Omega = (-10, 10)^2$  as sketched in Figure 1. In this domain, an initial crack with length  $l_0 = 2.0$  and thickness  $d$  of two cells on  $\Omega_c = [-1, 1] \times [-d, d] \subset \Omega$  is prescribed by help of the phase-field function  $\varphi$ , i.e.,  $\varphi = 0$  in  $\Omega_c$  and  $\varphi = 1$  in  $\Omega \setminus \Omega_c$ . Note that the thickness of  $2d$  corresponds to  $2h/\sqrt{2}$ , where  $h$  is the cell diameter. For the numerical realization,  $\varphi_h^0 = I_h^0(\varphi^0)$  is utilized.

As boundary conditions, the displacements  $u$  are set to zero on  $\partial\Omega$ . For the phase-field variable, we use homogeneous Neumann conditions (so-called traction free conditions), i.e.,  $\epsilon \partial_n \varphi = 0$  on  $\partial\Omega$ .

For all tests in the following sections the crack bandwidth  $\epsilon$  is set as  $\epsilon = 4\sqrt{2}d$ , the regularization parameter  $\kappa$  is determined sufficiently small with  $\kappa = 10^{-8}$ . The fracture toughness of the observed material is  $G_c = 1.0$  and the Young's modulus  $E = 1.0$ .

The numerical tests in the following are based on three configurations derived from Sneddon's setup as discussed in detail in [50] using the solving strategy described below for the discrete formulations of Section 3 and adaptively refined meshes based on the error estimator in Section 4:

- **Example 1:** Constant given pressure with  $p_g = 10^{-3}$  and  $\nu = 0.2$  to  $\nu = 0.5$  using Problem 3, called Example 1A, compared to Problem 4, called Example 1B, in Section 5.1;
- **Example 2:** Constant given pressure with  $p_g = 10^{-3}$ ,  $\nu = 0.2$  to  $\nu = 0.5$  and a compressible layer around the finite domain as well as in the prescribed fracture using Problem 3, called Example 2A, compared to Problem 4, called Example 2B, in Section 5.2, where details on the layer will be given;
- **Example 3:** Non-constant given pressure  $p_g$ ,  $\nu = 0.5$  and a compressible layer around the finite domain as well as in the prescribed fracture using Problem 4, called Example 3A, compared to Problem 5, called Example 3B, in Section 5.3.

### Solution algorithm

The coupled inequality system in Problems (3), 4, and 5 is formulated as a complementarity system as shown in [32]. Therein a Lagrange multiplier is introduced for treating the inequality constraint. The Lagrange multiplier  $\tau$  is discretized in the dual basis to the  $\mathbb{Q}_1$  space denoted by  $\mathbb{Q}_1^*$  and the corresponding discrete function space denoted as  $X_h$ .

The discrete form is then solved in a monolithic fashion, but noticing that  $\varphi$  is time-lagged in the first term of the displacement equation. This means in Problem 3, 4, and 5 we replace in (9), (7) and (12), respectively, the term  $g(\varphi_h)$  by  $g(\varphi_h^{n-1})$  and  $(\varphi_h^n)^2$  by  $(\varphi_h^{n-1})^2$ . This procedure helps in relaxing the nonlinearity. Of course, a temporal discretization error is introduced, which however is not significant in the steady-state tests considered here. To this end, we formulate a compact form by summing up all equations: Given the initial data  $\varphi^0$ ; for the loading steps  $n = 1, 2, \dots, N$ :

Find  $U_h := U_h^n = (u_h, p_h, \varphi_h, \tau_h) \in Y_h := (V_h \times P_h \times W_h \times X_h)$  such that

$$A_{\varphi^{n-1}}(u_h, p_h, \varphi_h, \tau_h) = 0.$$

To solve  $A_{\varphi^{n-1}}(\cdot) = 0$ , we formulate a residual-based Newton scheme, e.g., [49]. The concrete scheme (and its implementation) can be found in [19, 14]. The occurring linear systems are solved with a direct method provided by UMFPACK [13].

## Quantities of interest

For all examples, we compared the following quantities of interest:

- Total crack volume (TCV);
- Bulk energy  $E_b$ ;
- Crack energy  $E_c$ .

It will turn out for the discussion below, that focusing on TCV will be sufficient.

For the TCV, manufactured reference values can be computed for a infinite domain from the formulae presented in [42][Section 2.4]. Numerical values on the cut-off domain in Figure 1 and  $\nu = 0.2$  can be found in [50]. Numerically, the total crack volume can be computed by using

$$\text{TCV} = \int_{\Omega} u(x, y) \cdot \nabla \varphi(x, y) \, d(x, y). \quad (26)$$

Using the exact representation of  $u_y$  (cf. [42], page 29) applied to our parameter settings as in [50], we consequently obtain the reference values listed in Table 1 for an infinite domain.

Table 1: Manufactured reference values of the TCV computed by help of the formula in [50] for a infinite domain and different Poisson ratios up to the incompressible limit.

$\nu$	TCV <sub>2d</sub> (reference)
0.2	$6.03186 \times 10^{-3}$
0.49	$4.77459 \times 10^{-3}$
0.49999	$4.71245 \times 10^{-3}$
0.5	$4.71239 \times 10^{-3}$

As a second quantity of interest, the bulk energy  $E_b$  is defined as

$$E_b := \int_{\Omega} \frac{g(\phi)}{2} \sigma : e(u) dx, \quad (27)$$

where  $\sigma := \sigma(u)$  for Problem 3 and  $\sigma := \sigma(u, p)$  for Problem 4 and (5). As third quantity of interest, the crack energy is computed via

$$E_c := \frac{G_c}{2} \int_{\Omega} \left( \frac{(\varphi - 1)^2}{\epsilon} + \epsilon |\nabla \varphi|^2 \right) dx. \quad (28)$$

### 5.1 Sneddon-inspired test cases (Example 1)

In this first set of numerical examples, we compare Example 1A with Example 1B. The prescribed pressure is  $p_g = 10^{-3}$  and the Poisson ratios are  $\nu = 0.2, 0.49, 0.49999$  and  $\nu = 0.5$  (only for the mixed formulation Example 1B).

The starting meshes are once globally uniformly refined and three times further uniformly refined around the crack. The following three meshes are either uniformly refined in a zone around the crack (geometric refinement) or adaptively refined based on the estimator proposed in Section 4.

Table 2: The number of degrees of freedom (DoF) and the TCV for four different Poisson ratios for Example 1A and Example 1B.

$\nu$	$d$	Example 1A				Example 1B			
		geometric		adaptive		geometric		adaptive	
		DoF	TCV	DoF	TCV	DoF	TCV	DoF	TCV
0.2	0.0625	29,988	0.00818	29,988	0.00818	96,436	0.00821	96,436	0.00821
	0.03125	74,852	0.00691	36,964	0.00691	241,860	0.00693	118,916	0.00693
	0.015625	241,156	0.00639	49,044	0.00639	781,604	0.00640	157,900	0.00640
	0.0078125	880,740	0.00616	69,428	0.00616	2,858,788	0.00617	223,692	0.00617
0.49	0.0625	29,988	0.00601	29,988	0.00601	96,436	0.00620	96,436	0.00620
	0.03125	74,852	0.00492	36,580	0.00491	241,860	0.00504	117,668	0.00504
	0.015625	241,156	0.00440	48,436	0.00438	781,604	0.00448	155,948	0.00447
	0.0078125	880,740	0.00415	68,628	0.00413	2,858,788	0.00421	221,116	0.00421
0.49999	0.0625	29,988	2.28E-5	29,988	2.28E-5	96,436	2.38E-5	96,436	2.38E-5
	0.03125	74,852	2.33E-5	37,332	2.29E-5	241,860	2.39E-5	120,124	2.39E-5
	0.015625	241,156	2.35E-5	47,844	2.28E-5	781,604	2.39E-5	154,036	2.39E-5
	0.0078125	880,740	2.36E-5	70,164	2.28E-5	2,858,788	2.39E-5	226,108	2.39E-5
0.5	0.0625					96,436	1.44E-5	96,436	1.44E-5
	0.03125					241,860	-1.15E-6	118,292	-2.03E-7
	0.015625					781,604	-1.29E-7	155,284	-1.33E-7
	0.0078125					2,858,788	-3.38E-8	227,356	-3.46E-8

Tables 2 and 3 show the resulting values for the TCV and  $E_b$  on the starting mesh and the following three geometrically or adaptively refined meshes with adjusted parameters  $\epsilon$  and  $d$  according to [50].

*Remark 3* Considering adaptively refined meshes, the parameters  $\epsilon$  and  $d$  are decreased by a factor of two after each refinement. Hence these values are the same for the computations on geometrically refined meshes, which allows a fair comparison of results coming from geometrically and adaptively refined meshes.

Table 3: The number of degrees of freedom (DoF) and the bulk energy  $E_b$  for four different Poisson ratios for Example 1A and Example 1B.

$\nu$	$d$	Example 1A				Example 1B			
		geometric		adaptive		geometric		adaptive	
		DoF	$E_b$	DoF	$E_b$	DoF	$E_b$	DoF	$E_b$
0.2	0.0625	29,988	4.06E-6	29,988	4.06E-6	96,436	4.07E-6	96,436	4.07E-6
	0.03125	74,852	3.38E-6	36,964	3.38E-6	241,860	3.39E-6	118,916	3.39E-6
	0.015625	241,156	3.14E-6	49,044	3.13E-6	781,604	3.14E-6	157,900	3.14E-6
	0.0078125	880,740	3.04E-6	69,428	3.04E-6	2,858,788	3.05E-6	223,692	3.05E-6
0.49	0.0625	29,988	3.00E-6	29,988	3.00E-6	96,436	3.09E-6	96,436	3.09E-6
	0.03125	74,852	2.46E-6	36,580	2.45E-6	241,860	2.52E-6	117,668	2.52E-6
	0.015625	241,156	2.20E-6	48,436	2.19E-6	781,604	2.23E-6	155,948	2.23E-6
	0.0078125	880,740	2.08E-6	68,628	2.06E-6	2,858,788	2.10E-6	221,116	2.10E-6
0.49999	0.0625	29,988	1.14E-8	29,988	1.14E-8	96,436	1.19E-8	96,436	1.19E-8
	0.03125	74,852	1.16E-8	37,332	1.14E-8	241,860	1.19E-8	120,124	1.19E-8
	0.015625	241,156	1.17E-8	47,844	1.14E-8	781,604	1.19E-8	154,036	1.19E-8
	0.0078125	880,740	1.18E-8	70,164	1.14E-8	2,858,788	1.19E-8	226,108	1.19E-8
0.5	0.0625					96,436	4.06E-9	96,436	4.06E-9
	0.03125					241,860	-3.25E-10	118,292	-5.74E-11
	0.015625					781,604	-3.65E-11	155,284	-3.76E-11
	0.0078125					2,858,788	-9.56E-12	227,356	-9.77E-12

For  $\nu = 0.2$  the TCV and  $E_b$  computed with Problem 3, rounded to three significant digits, matches the numbers given in [50], hence we conclude the correctness of our implementation.

The fracture energy  $E_c$  is identical to the values in [50]. On the coarsest mesh this corresponds to  $E_c \approx 2.895$  and on the finest mesh we have  $E_c \approx 2.423$ . As the numbers for  $E_c$  are independent of  $\nu$  and the chosen formulation, they are not listed separately.

In the following, we will focus on the behavior of TCV for different Poisson ratios and compare it to the reference values of Table 1 on an infinite domain. First, we see in Table 2 and Table 3 that both quantities of interest are numerically stable under mesh refinement. This shows the robustness of our proposed models and their numerical realization. Second, we observe that more incompressible materials yield smaller values of the TCV much smaller than the predicted values in Table 1. Physically, this is to be expected if we think of incompressible material in a closed box, because the material cannot move. Due to the cut-off of the computational domain and the use of an incompressible material, no movement can be expected for  $\nu \approx 0.5$ . This led us to suggest the setting of Section 5.2 where we add an artificial compressible

layer around the (nearly) incompressible domain and inside the prescribed fracture  $(-1, 1) \times (-d, d)$ .

## 5.2 Incompressible material surrounded with a compressible layer (Example 2)

As we have seen in the previous example in terms of the total crack volume, for  $\nu_s = 0.49999$ , the fracture in incompressible solids will not open anymore and the TCV is almost 0. On the other hand, the formulae in [42][Section 2.4] suggest a value greater than zero. The reason being that therein an infinite domain was assumed. To study incompressible solids in larger domains, we use a trick and add a compressible layer as surrounding area. Considering Figure 1, now we work in a domain  $(-20, 20)^2$  which contains the previously defined domain  $(-10, 10)^2$ . The surrounding layer of width 10 is defined as a compressible material with  $\nu = 0.2$ . All other parameters, namely  $E$ ,  $G_c$ ,  $\kappa$  and  $\Omega_c$  are kept as before with the values listed in the first paragraph of Section 5. The same compressible material is used inside of the prescribed fracture on the set  $(-1, 1) \times (-d, d)$ .

In Figure 2, the ranges of the  $x$ - and the  $y$ - displacements as well as for the pressure values are depicted for Example 2B, where a perfect symmetry of the test setup can be observed.

In Table 4, for the primal-based form (Example 2A), the TCV is underestimated for  $\nu \approx 0.5$  while the mixed form (Example 2B) gives results consistent with the computations for  $\nu = 0.5$ . Compared to Table 1, the TCV values based on the mixed form (Example 2B) are very similar for the four listed Poisson ratios compared to the reference values. Keep in mind at this point, that the reference values are given analytically considering an infinite domain.

Further, the TCV in Table 4 on adaptively refined meshes in comparison to geometrically refined meshes coincide satisfactorily. Note however, that as it has to be expected the primal formulation (3) provides unreliable values for  $\nu$  close to 0.5.

To give an impression of the used meshes and to see the difference between geometrically and adaptively refined meshes, in Figure 3, a coarser starting mesh (geometrically pre-refined) on the left and the mesh after three additional adaptive refinements (based on the error estimator) on the right are given. Thinking of the problem size and workload, the adaptively refined meshes by help of the error estimator of Section 4 just needs a tenth of the DoFs, but yields very similar results for the TCV on the finest refinement level.



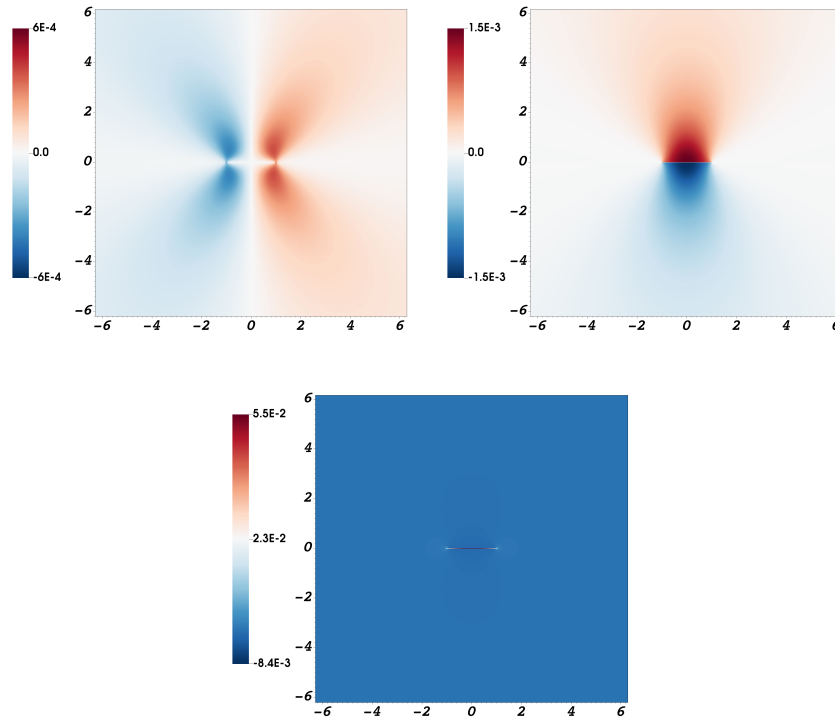


Fig. 2: Example 2B: The  $x$ - and  $y$ -displacements and the pressure  $p$  for  $\nu = 0.5$ .

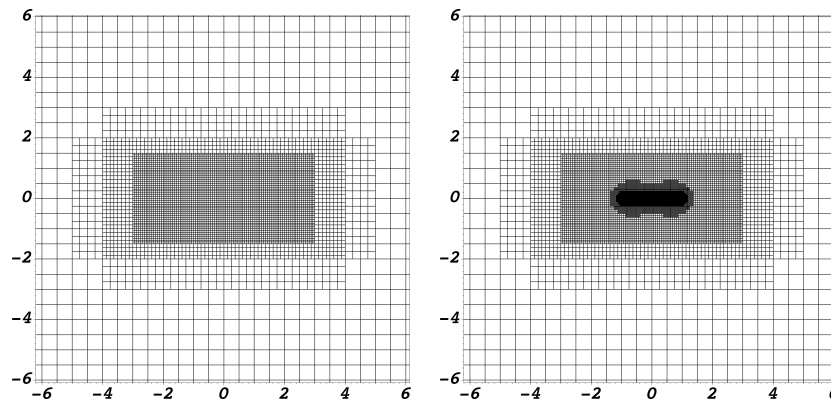


Fig. 3: The mesh on the starting grid (left) and after three levels of adaptive refinement (right) for Example 2B with  $\nu = 0.5$  zoomed to the crack zone.

Table 4: The number of degrees of freedom (DoF) and the TCV for four different Poisson ratios for Example 2A and Example 2B.

$\nu$	$d$	Example 2A				Example 2B			
		geometric		adaptive		geometric		adaptive	
		DoF	TCV	DoF	TCV	DoF	TCV	DoF	TCV
0.2	0.0625	49,508	0.00836	49,508	0.00836	159,316	0.00839	159,316	0.00839
	0.03125	94,372	0.00703	58,036	0.00702	304,740	0.00704	186,828	0.00704
	0.015625	260,676	0.00648	72,420	0.00648	844,484	0.00649	233,300	0.00649
	0.0078125	900,260	0.00624	93,220	0.00624	2,921,668	0.00625	300,420	0.00625
0.49	0.0625	49,508	0.00808	49,508	0.00808	159,316	0.00842	159,316	0.00842
	0.03125	94,372	0.00622	58,420	0.00620	304,740	0.00640	188,076	0.00640
	0.015625	260,676	0.00540	72,804	0.00537	844,484	0.00551	234,548	0.00551
	0.0078125	900,260	0.00503	93,796	0.00500	2,921,668	0.00511	301,668	0.00511
0.49999	0.0625	49,508	0.000913	49,508	0.000913	159,316	0.00840	159,316	0.00840
	0.03125	94,372	0.00129	57,236	0.000890	304,740	0.00636	188,076	0.00636
	0.015625	260,676	0.00188	71,044	0.000860	844,484	0.00545	234,548	0.00545
	0.0078125	900,260	0.00237	91,220	0.000838	2,921,668	0.00505	301,668	0.00505
0.5	0.0625					159,316	0.00840	159,316	0.00840
	0.03125					304,740	0.00636	188,076	0.00636
	0.015625					844,484	0.00545	234,548	0.00545
	0.0078125					2,921,668	0.00505	301,668	0.00505

### 5.3 Nonhomogeneous pressure test case with a compressible layer (Example 3)

In this third example, we prescribe a nonhomogeneous pressure  $p_g$  in form of a bump that resembles to a fluid-filled fracture situation (e.g., [34]). In this situation, we can no longer expect our pressure  $p$  to be almost constant. As it has been observed, e.g., in [28, 29] for Stokes flow, for incompressible situations the difficulty in approximating the pressure can negatively influence the approximation of the displacement field. Hence, for the third example, we will focus on the case  $\nu = 0.5$  and compare the numerical results from Problem 4 with the pressure robust Problem 5.

For this setting we consider the following given pressure:

$$p_g(x, y) = f(x)g(y)$$

where

$$f(x) = \begin{cases} 0.001 & 1 \leq x < 2, \\ -0.002 x^2(x - 1.5) & 0 \leq x < 1, \\ 0.002 (x - 3)^2(x - 1.5) & 2 \leq x < 3, \\ 0 & \text{otherwise,} \end{cases}$$

$$g(y) = \begin{cases} 1 & |y| < 0.5, \\ 2(|y| - 1.5)^2|y| & 0.5 \leq |y| < 1.5, \\ 0 & \text{otherwise.} \end{cases}$$

All other parameters are chosen as in Example 2.

The solution is shown in Figure 4, where the nonsymmetry in the setup can be clearly seen in the  $x$ -displacements. It should be noted that similar to Example 2 the

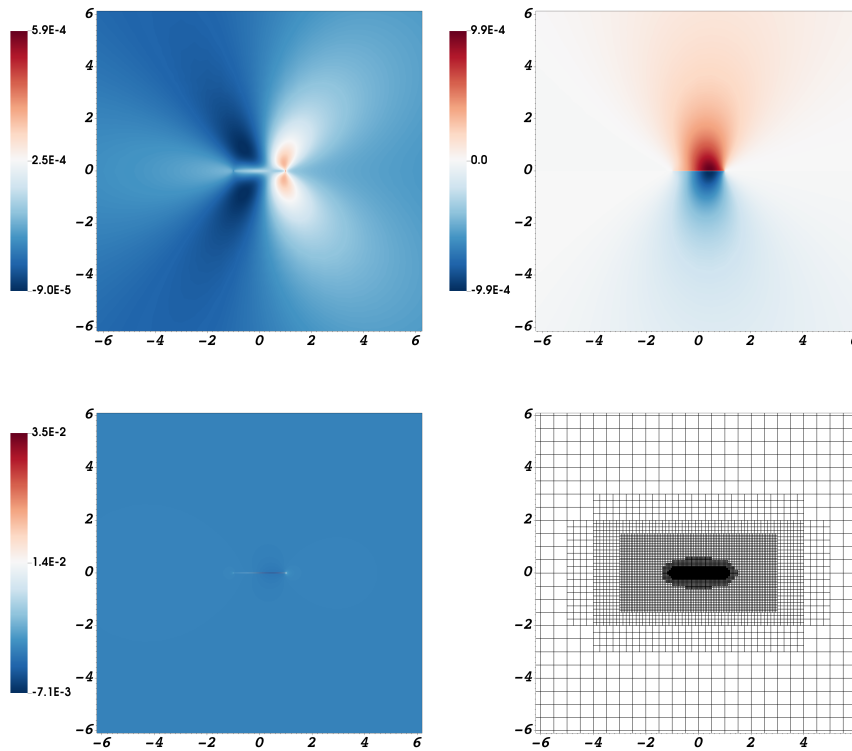


Fig. 4: Example 3: The  $x$ - and  $y$ -displacements (top row), and the pressure  $p$  for  $\nu = 0.5$  and the final locally adapted mesh.

pressure is relatively simple, and the jump in the pressure on the prescribed fracture is aligned with the mesh. Hence, no difficulty in the pressure approximation is expected

- and thus the pressure robust results should not deviate too much. Indeed, as the numbers in Table 5 show the pressure robust discretization yields similar numerical results. This is not visible in the table, but actual numbers differ in later digits.

Table 5: The number of degrees of freedom (DoF) and the TCV for Example 3A and Example 3B.

		Example 3A				Example 3B			
$\nu$	$d$	geometric		adaptive		geometric		adaptive	
		DoF	TCV	DoF	TCV	DoF	TCV	DoF	TCV
0.5	0.0625	159,316	0.00372	159,316	0.00372	159,316	0.00372	159,316	0.00372
	0.03125	304,740	0.00314	187,744	0.00314	304,740	0.00314	187,744	0.00314
	0.015625	844,484	0.00273	233,280	0.00273	844,484	0.00273	233,280	0.00273
	0.0078125	2,921,668	0.00252	299,092	0.00252	2,921,668	0.00252	299,092	0.00252

Since the given pressure only enters the equation on the boundary of the approximate fracture, i.e., the region where  $\nabla\phi \neq 0$ , this rather similar behavior of Problem 4 and 5 has to be expected. It remains subject to future research if this remains the same for growing fractures of other forcings.

## 6 Conclusions

In this work, we developed a pressurized phase-field fracture model in mixed form for solids up to the incompressible limit  $\nu = 0.5$ . In addition, a residual-type error estimator is presented for the variational inequality, in this context especially for fractures in solids which are (nearly) incompressible. Estimating the error in the phase-field variable allows to obtain a good resolution especially of the fracture zone.

We investigated the performance of the mixed phase-field fracture formulation and the error estimator with the help of three numerical configurations, all based on Sneddon's and Lowengrub's setup [42] and [41]. The theoretical calculations therein based on an infinite pressure-driven cavity and in particular an exact formula for the total crack volume, in this work is mainly used to prove the quality of the mixed form as well as the adaptive refinement based on the error estimator.

In a second numerical configuration we added a compressible layer around the (nearly) incompressible cavity to allow computing similar results for the TCV as given by the exact formula on an infinite domain. The findings observed on a compressible layered cavity, which is incompressible in the inner square and around the crack zone, are very convincing. To go even further, as a third numerical example, we added a non-constant pressure to the layered Sneddon configuration to provide results of a configuration which is not totally symmetric and tested the results in

comparison with a pressure robust modification. It turned out that in the benchmark setup the pressure approximation has no significant influence on the displacement fields and thus a pressure robust discretization is not necessary. It will be subject to further studies to check if the situation remains similar considering a fracture which is not only opening in width but also growing in length.

**Acknowledgements** Funded by the Deutsche Forschungsgemeinschaft (DFG, German Research Foundation) – Projektnummer 392587580

## References

1. L. AMBROSIO AND V. TORTORELLI, *Approximation of functionals depending on jumps by elliptic functionals via  $\gamma$ -convergence*, Comm. Pure Appl. Math., 43 (1990), pp. 999–1036.
2. ———, *On the approximation of free discontinuity problems*, Boll. Un. Mat. Ital. B, 6 (1992), pp. 105–123.
3. D. ARNDT, W. BANGERTH, T. C. CLEVINGER, D. DAVYDOV, M. FEHLING, D. GARCIA-SANCHEZ, G. HARPER, T. HEISTER, L. HELTAI, M. KRONBICHLER, R. M. KYNCH, M. MAIER, J.-P. PELTERET, B. TURCK SIN, AND D. WELLS, *The deal.II library, version 9.1*, Journal of Numerical Mathematics, 27 (2019), pp. 203–213.
4. M. ARTINA, M. FORNASIER, S. MICHELETTI, AND S. PEROTTO, *Anisotropic mesh adaptation for crack detection in brittle materials*, SIAM J. Sci. Comput., 37 (2015), pp. B633–B659.
5. W. BANGERTH, R. HARTMANN, AND G. KANSCHAT, *deal.II – a general purpose object oriented finite element library*, ACM Trans. Math. Softw., 33 (2007), pp. 24/1–24/27.
6. B. BOURDIN, G. FRANCFORT, AND J.-J. MARIGO, *Numerical experiments in revisited brittle fracture*, J. Mech. Phys. Solids, 48 (2000), pp. 797–826.
7. D. BRAESS, *Finite Elemente*, Springer-Verlag Berlin Heidelberg, Berlin, Heidelberg, vierte, überarbeitete und erweiterte ed., 2007.
8. F. BREZZI AND M. FORTIN, *Mixed and Hybrid Finite Element Methods*, vol. 15 of Springer Series in Computational Mathematics, Springer-Verlag, 1991.
9. M. K. BRUN, T. WICK, I. BERRE, J. M. NORDBOTTEN, AND F. A. RADU, *An iterative staggered scheme for phase field brittle fracture propagation with stabilizing parameters*, Computer Methods in Applied Mechanics and Engineering, 361 (2020), p. 112752.
10. S. BURKE, C. ORTNER, AND E. SÜLLI, *An adaptive finite element approximation of a variational model of brittle fracture*, SIAM J. Numer. Anal., 48 (2010), pp. 980–1012.
11. ———, *An adaptive finite element approximation of a generalized Ambrosio-Tortorelli functional*, M3AS, 23 (2013), pp. 1663–1697.
12. C. CHUKWUDOZIE, B. BOURDIN, AND K. YOSHIOKA, *A variational phase-field model for hydraulic fracturing in porous media*, Computer Methods in Applied Mechanics and Engineering, 347 (2019), pp. 957 – 982.
13. T. A. DAVIS AND I. S. DUFF, *An unsymmetric-pattern multifrontal method for sparse LU factorization*, SIAM J. Matrix Anal. Appl., 18 (1997), pp. 140–158.
14. *The Differential Equation and Optimization Environment: DOpELIB*. <http://www.dopelib.net>.
15. C. ENGWER, S. I. POP, AND T. WICK, *Dynamic and weighted stabilizations of the l-scheme applied to a phase-field model for fracture propagation*. arXiv:1912.07096, 2019.
16. M. FAN, Y. JIN, AND T. WICK, *A phase-field model for mixed-mode fracture*. Hannover : Institutionelles Repositorium der Leibniz Universität Hannover, 2019, 40 S. DOI: <https://doi.org/10.15488/5369>, 2019.
17. F. FIERRO AND A. VEESER, *A posteriori error estimators for regularized total variation of characteristic functions*, SIAM J. Numer. Anal., 41 (2003), pp. 2032–2055 (electronic).

18. G. FRANCFORT AND J.-J. MARIGO, *Revisiting brittle fracture as an energy minimization problem*, J. Mech. Phys. Solids, 46 (1998), pp. 1319–1342.
19. C. GOLL, T. WICK, AND W. WOLLNER, *DOPelib: Differential equations and Optimization Environment; A goal oriented software library for solving PDEs and optimization problems with PDEs*, Archive of Numerical Software, 5 (2017), pp. 1–14.
20. Y. HEIDER, S. REICHE, P. SIEBERT, AND B. MARKERT, *Modeling of hydraulic fracturing using a porous-media phase-field approach with reference to experimental data*, Engineering Fracture Mechanics, 202 (2018), pp. 116 – 134.
21. T. HEISTER, M. F. WHEELER, AND T. WICK, *A primal-dual active set method and predictor-corrector mesh adaptivity for computing fracture propagation using a phase-field approach*, Comp. Meth. Appl. Mech. Engrg., 290 (2015), pp. 466 – 495.
22. T. HEISTER AND T. WICK, *Parallel solution, adaptivity, computational convergence, and open-source code of 2d and 3d pressurized phase-field fracture problems*, PAMM, 18 (2018), p. e201800353.
23. G. A. HOLZAPFEL, *Nonlinear solid mechanics: a continuum approach for engineering science*, Meccanica, 37 (2002), pp. 489–490.
24. G. A. HOLZAPFEL, R. EBERLEIN, P. WRIGGERS, AND H. W. WEIZSÄCKER, *Large strain analysis of soft biological membranes: Formulation and finite element analysis*, Computer Methods in Applied Mechanics and Engineering, 132 (1996), pp. 45–61.
25. R. KRAUSE, A. VEESER, AND M. WALLOTH, *An efficient and reliable residual-type a posteriori error estimator for the Signorini problem*, Numerische Mathematik, 130 (2015), pp. 151–197.
26. A. KUBO AND Y. UMEMO, *Velocity mode transition of dynamic crack propagation in hyperviscoelastic materials: A continuum model study*, Scientific Reports, 7 (2017), p. 42305.
27. S. LEE, M. F. WHEELER, AND T. WICK, *Pressure and fluid-driven fracture propagation in porous media using an adaptive finite element phase field model*, Computer Methods in Applied Mechanics and Engineering, 305 (2016), pp. 111 – 132.
28. A. LINKE, G. MATTHIES, AND L. TOBISKA, *Robust arbitrary order mixed finite element methods for the incompressible Stokes equations with pressure independent velocity errors*, M2AN Math. Model. Numer. Anal., 50 (2016), pp. 289–309.
29. A. LINKE, C. MERDON, AND W. WOLLNER, *Optimal  $L^2$  velocity error estimates for a modified pressure-robust Crouzeix-Raviart Stokes element*, IMA J. Numer. Anal., 37 (2017), pp. 354–374.
30. K. MANG, M. WALLOTH, T. WICK, AND W. WOLLNER, *Mesh adaptivity for quasi-static phase-field fractures based on a residual-type a posteriori error estimator*, GAMM Mitteilungen, (2019). Early-Access.
31. ———, *Adaptive numerical simulation of a phase-field fracture model in mixed form tested on an I-shaped specimen with high poisson ratios*, 2020.
32. K. MANG, T. WICK, AND W. WOLLNER, *A phase-field model for fractures in nearly incompressible solids*, Computational Mechanics, 65 (2020), pp. 61–78.
33. C. MIEHE, S. MAUTHE, AND S. TEICHTMEISTER, *Minimization principles for the coupled problem of darcy-Åšbiot-type fluid transport in porous media linked to phase field modeling of fracture*, Journal of the Mechanics and Physics of Solids, 82 (2015), pp. 186 – 217.
34. A. MIKELIĆ, M. F. WHEELER, AND T. WICK, *Phase-field modeling of a fluid-driven fracture in a poroelastic medium*, Computational Geosciences, 19 (2015), pp. 1171–1195.
35. A. MIKELIĆ, M. F. WHEELER, AND T. WICK, *A quasi-static phase-field approach to pressurized fractures*, Nonlinearity, 28 (2015), pp. 1371–1399.
36. A. MIKELIĆ, M. F. WHEELER, AND T. WICK, *Phase-field modeling through iterative splitting of hydraulic fractures in a poroelastic medium*, GEM - International Journal on Geomathematics, 10 (2019).
37. K.-S. MOON, R. H. NOCHETTO, T. VON PETERSDORFF, AND C.-S. ZHANG, *A posteriori error analysis for parabolic variational inequalities*, M2AN. Mathematical Modelling and Numerical Analysis, 41 (2007), pp. 485–511.
38. N. NOII, F. ALDAKHEEL, T. WICK, AND P. WRIGGERS, *An adaptive global-local approach for phase-field modeling of anisotropic brittle fracture*, Computer Methods in Applied Mechanics and Engineering, (2019), p. 112744.

39. N. NOH AND T. WICK, *A phase-field description for pressurized and non-isothermal propagating fractures*, Computer Methods in Applied Mechanics and Engineering, 351 (2019), pp. 860 – 890.
40. J. SCHRÖDER, P. NEFF, AND D. BALZANI, *A variational approach for materially stable anisotropic hyperelasticity*, International Journal of Solids and Structures, 42 (2005), pp. 4352–4371.
41. I. N. SNEDDON, *The distribution of stress in the neighbourhood of a crack in an elastic solid*, Proc. R. Soc. Lond. A, 187 (1946), pp. 229–260.
42. I. N. SNEDDON AND M. LOWENGRUB, *Crack problems in the classical theory of elasticity*, SIAM series in Applied Mathematics, John Wiley and Sons, Philadelphia, 1969.
43. R. TAYLOR, *Isogeometric analysis of nearly incompressible solids*, International Journal for Numerical Methods in Engineering, 87 (2011), pp. 273–288.
44. M. WALLOTH, *Residual-type a posteriori estimators for a singularly perturbed reaction-diffusion variational inequality – reliability, efficiency and robustness*, Tech. Rep. 1812.01957, arXiv, 2018.
45. M. WALLOTH, *Residual-type a posteriori error estimator for a quasi-static Signorini contact problem*, IMA Journal of Numerical Analysis, (2019). <https://doi.org/10.1093/imanum/drz023>.
46. M. WHEELER, T. WICK, AND W. WOLLNER, *An augmented-Lagrangian method for the phase-field approach for pressurized fractures*, Comp. Meth. Appl. Mech. Engrg., 271 (2014), pp. 69–85.
47. M. F. WHEELER, T. WICK, AND S. LEE, *Ipacs: Integrated phase-field advanced crack propagation simulator. an adaptive, parallel, physics-based-discretization phase-field framework for fracture propagation in porous media*, Computer Methods in Applied Mechanics and Engineering, 367 (2020), p. 113124.
48. T. WICK, *Goal functional evaluations for phase-field fracture using PU-based DWR mesh adaptivity*, Computational Mechanics, 57 (2016), pp. 1017–1035.
49. ———, *An error-oriented Newton/inexact augmented Lagrangian approach for fully monolithic phase-field fracture propagation*, SIAM Journal on Scientific Computing, 39 (2017), pp. B589–B617.
50. T. WICK, R. MÜLLER, S. KOLLMANNBERGER, M. KÄSTNER, P. HENNIG, E. RANK, M. ELHAD-DAD, D. D’ANGELLA, C. KUHN, T. HEISTER, K. MANG, M. WALLOTH, W. WOLLNER, A. SCHWARZ, AND J. SCHRÖDER, *A selection of benchmark problems in solid mechanics and applied mathematics: Part II*, 2020. in preparation.